A G-band Radar for Humidity and Cloud Remote Sensing

A G-band Radar for Humidity and Cloud Remote Sensing

Ken B. Cooper, Richard Roy, Robert Dengler, Raquel Rodriguez Monje, Maria Alonso-delPino, Jose Siles, Okan Yurduseven, Chaitali Parashare, Luis Millán, and Matthew Lebsock

***Abstract*— VIPR (Vapor In-cloud Profiling Radar) is a tunable G-band radar designed for humidity and cloud remote sensing. Using all-solid-state components and operating in a frequency-modulated continuous-wave (FMCW) radar mode, VIPR's transmit power is 200-300 mW. Its typical chirp bandwidth of 10 MHz over a center-frequency tuning span of 167-174.8 GHz results in a nominal range resolution of 15 m. The radar's measured noise figure over the transmit band is between 7.4-10.4 dB, depending on its frequency and hardware configuration, and its calculated antenna gain is 58 dB. These parameters mean that with typical 1 ms chirp times, single-pulse cloud reflectivities as low as -26 dBZ are detectable with unity signal-to-noise at 5 km. Experimentally, radar returns from ice clouds above 10 km in height have been observed from the ground. VIPR's absolute sensitivity was validated using a spherical metal target in the radar antenna's far field, and a G-band switch has been implemented in an RF calibration loop for periodic recalibration. The radar achieves high sensitivity with thermal noise limited detection by virtue of both its low-noise RF architecture and by using a quasioptical duplexing method that preserves ultra-high transmit/receive isolation despite operation in an FMCW mode with a single primary antenna shared by the transmitter and receiver.**

***Index Terms*— airborne radar, differential absorption radar, meteorological radar, millimeter wave radar.**

I. Introduction

RADAR systems operating at frequencies above W-band are uncommon because of the lack of available technology, yet they offer several attractive capabilities for atmospheric remote sensing applications [1]. Their small wavelengths scatter strongly from small hydrometers, and when operating concurrently with lower frequency radars, high-frequency radars will often encounter non-Rayleigh scattering, allowing inferences of possible particle size distributions to be made. Small wavelengths offer larger bandwidths and higher antenna gain (for a fixed aperture size), hence better range and cross-range resolution limits of a probed volume. They are more sensitive to low-velocity Doppler shifts or low-amplitude "micro-Doppler" vibrations. Millimeter-wave radars above 100 GHz can also be used to measure atmospheric transmission properties that derive from the prominent spectroscopic absorption lines of gaseous constituents, primarily water vapor and oxygen.

On the other hand, high-frequency radars face two significant drawbacks: large attenuation through moist or precipitating volumes, and the high cost or outright lack of basic RF components. In terms of propagation loss, ground-level one-way attenuation in the 230 GHz atmospheric transmission window, for example, can vary from less than 0.5 dB/km to more than 10 dB/km, depending on humidity conditions [2]. (For radar applications, one-way attenuation values must be doubled for two-way beam path calculations.) Attenuation becomes more severe at higher RF frequencies. Around 680 GHz, where radar and communication systems have been demonstrated on an experimental basis [3, 4], absorption as high as 200 dB/km is possible under humid conditions even though this frequency is an atmospheric transmission *window*.

Radar beam extinction from clouds is also more attenuating at higher frequencies, although simple expressions involving Rayleigh scattering become less applicable above about 50 GHz as Mie scattering effects become prominent in all but non-precipitating liquid water clouds. In [5], calculations done for typical 0.8 g/m^3 stratus clouds are summarized showing that total extinction increases from about 5 dB/km to over 20 dB/km as the propagation frequency triples from 100 to 300 GHz. Non-Rayleigh scattering is even more prominent for rain, since drop sizes are larger, and [5] describes how extinction through rain is fairly flat with frequency in the 100-1000 GHz span, with values reaching 10 dB/km for rainfall conditions of ~20 mm/hr.

RF component availability, meanwhile, diminishes as frequencies exceed 100 GHz and the "THz gap" is entered. To be sure, research groups worldwide have made significant strides in the last 20 years in pushing the limits of high-frequency electronics, whether that be digital-based silicon CMOS or BiCMOS circuits [6, 7, 8] or III-V semiconductors [9, 10, 11]. Such components have already been demonstrated in short-range detection and imaging applications. However,

Manuscript received October 5, 2019. This research was supported in part by NASA's Earth Science Technology Office under the Instrument Incubator Program, and was carried out at the Jet Propulsion Laboratory (JPL), California Institute of Technology, Pasadena, CA, USA, under contract with the National Aeronautics and Space Administration.

This research was also supported by the Atmospheric Radiation Measurement (ARM) User Facility, a U.S. Department of Energy (DOE) Office of Science user facility managed by the Office of Biological and Environmental Research. Data were obtained from the Atmospheric Radiation Measurement (ARM) User Facility, a U.S. Department of Energy (DOE) Office of Science user facility managed by the Office of Biological and Environmental Research.

All authors with the exception of O.Y. are with the Jet Propulsion Laboratory, California Institute of Technology, Pasadena, CA 91109 USA (e-mail: ken.b.cooper@jpl.nasa.gov). O. Y. is with the Institute of Electronics, Communications and Information Technology (ECIT), Queen's University Belfast, Belfast BT3 9DT, UK (okan.yurduseven@qub.ac.uk).

without a significant commercial or defense market, extremely high-frequency radars will remain specialty products with limited availability and relatively high cost.

For all the above reasons, G-band (110-300 GHz) radars, being in the next highest designated interval above W-band, will most naturally be exploited first for atmospheric measurements. A recent article by Battaglia [1] persuasively describes how microphysical properties of a variety of clouds and precipitation with millimeter-range hydrometer sizes can be inferred from Doppler and multi-frequency radar measurements at G-band. To reach these atmospheric measurement objectives, two general categories of G-band radars are 1) high-transmit-power pulsed radars that use high-voltage vacuum electronic sources such as klystrons or traveling wave tubes, and 2) low-power high-gain-compression radars composed only of solid-state active devices. An example of the former is the DARPA-initiated Video Synthetic Aperture Radar (ViSAR) program that operates at 235 GHz and generates sufficient power for imaging ground-based targets from aircraft through clouds [12]. A vacuum-electronic RF source at G-band was also used by the University of Massachusetts, Amherst, to study clouds, fog, and terrain backscattering near 215 GHz [13, 14].

In the category of low-power solid-state G-band radars appropriate for atmospheric measurements, the 167-174.8 GHz VIPR (Vapor In-cloud Profiling Radar) system built by our group at the Jet Propulsion Laboratory (JPL) is the only one, to our knowledge, that has been designed specifically for remote sensing measurements of the atmosphere. VIPR began as a breadboard "proof-of-concept" radar operating over 183-193 GHz [15]. Since then, it has been modified to operate at lower frequencies [16], upgraded with a larger antenna and higher transmit power, validated for its humidity profiling capabilities at the Department of Energy's Southern Great Plains – Atmospheric Radiation Measurement (SGP-ARM) facility [17], and deployed from an aircraft in a downward-viewing configuration.

VIPR performs three primary measurements: range-resolved absolute humidity profiling within volumes of clouds or precipitation; total or partial column water vapor sounding in clear air between the radar and a distant target such as cloud cover; and reflectivity detection from clouds and precipitation. In this paper, we describe the architecture and performance of VIPR, including its major radar parameter characteristics, an RF block diagram and optical feed system designed for low noise detection, signal processing and calibration techniques, and some cloud and humidity profiling measurement results.

II. VIPR High-Level System Architecture

A. Choice of Radar Transmit Frequency

The principle of differential absorption radar (DAR) for humidity sounding inside clouds and precipitation has been explained previously [18, 19, 16]. Briefly, the DAR technique uses frequency sweeping or switching over a substantial bandwidth near the flank of a strong water vapor absorption line, for example the prominent one centered at 183.3 GHz. Ratios of the detected radar echo powers from clouds or rain are measured for different transmit frequencies that are either "on-line" or "off-line," which in practice are at two different positions higher and lower along the water line's flank. This ratio in the measured radar echo strength is hence a measure of the water vapor density in the beam path. The frequency-based echo power ratios are then further ratioed from different ranges along the beam path, which cancels out common-mode hardware-dependent radar characteristics and spatial (though not frequency) dependences of cloud scattering. This combination of four individual echo power measurements allows the specific atmospheric attenuation as a function of distance to be inferred and used to calculate profiles of absolute humidity based on well-understood atmospheric propagation models. Importantly, DAR is a *calibration-free* measurement, as long as the following assumptions hold: 1) the frequency-dependence of the radar beam's propagation attenuation is dominated by water vapor, rather than extinction and scattering from the hydrometers inside clouds and rain, and 2) that the on- and off-line measurements probe the same scene.

If frequency allocation restrictions were ignored (impossible in practice), the ideal frequency tuning for a DAR system near 183 GHz depends on the atmospheric conditions being probed. For example Figure 1 shows a calculation (using a model from [20]) of typical mid-latitude atmospheric one-way attenuation as a function of frequency near 183 GHz and altitude.

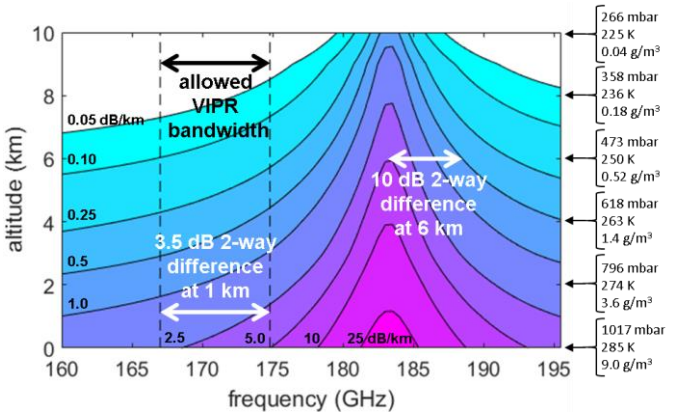

Figure 1. The contour plot shows calculated one-way atmospheric absorption as a function of altitude and frequency for typical mid-latitude conditions (temperature, pressure, and absolute humidity indicated on the right axis). VIPR's measurements are most accurate with a ~10 dB/km two-way differential specific absorption. Restricted to the 167-174.8 GHz band by frequency allocation regulations, VIPR is most sensitive to humidity in the Planetary Boundary Layer below ~2 km altitude.

As a rough rule of thumb based on both experimentation and our models of DAR detection sensitivity, to measure humidity profiles with sub-kilometer resolution over multi-kilometer spans, the difference between a two-way on-line and off-line attenuation values should be of order ~10 dB/km. For example, using the uncertainty analysis in [16], we find that 10 dB/km two-way differential absorption yields humidity profiling estimates at 200 m resolution with ~10% precision when averaging 2000 uncorrelated measurements. The differential attenuation optimum comes from a compromise between high absorption contrast achieved with the on-line tone far up the

absorption peak, and high signal-to-noise which favors frequencies away from the peak. Referring to Figure 1, if mid-tropospheric ice clouds around an altitude of 6 km were targeted, a DAR system should be tuned over ~5 GHz just above (or below) the 183 GHz line peak. In contrast, VIPR operates only in the 167-174.8 GHz range under a temporary experimental transmission permit. This compromises VIPR's potential sensitivity, and it means that the instrument is most sensitive to lower-altitude humidity levels. At 1 km altitude, for example, Figure 1 shows a two-way attenuation difference of 3.5 dB with smaller values at higher altitudes.

B. Major Radar Performance Parameters and Sensitivity

After the transmit frequency range choice, the primary hardware drivers of VIPR's performance are its aperture size, transmit power, receiver sensitivity, and waveform modulation strategy. VIPR's *single* primary aperture diameter of 60 cm, shared by the transmit and receive horn, was chosen to be as large as could be accommodated by the aircraft platform that has been used to test the instrument in late 2019 and early 2020, a DHC-6-300 from Twin Otter International Ltd. This aircraft features a large open-air nadir viewport from which VIPR can probe clouds and rain from above, as a demonstration for future satellite-based observation methods. The absence of any kind of radome or window (as in a hypothetical spaceborne application) is important to maximize the radar's sensitivity because transmit/receive (T/R) isolation levels exceeding 80 dB are necessary to prevent phase noise carried by near-zero-range reflections from increasing the system thermal noise level, as described in Section IIIB. Achieving such high isolation also requires a significant -30 dB edge taper for the antenna illumination, resulting in a radar antenna gain of 57.8 dB (0.25° full-width half-power beam).

For transmit power, VIPR uses the highest-power continuous-wave semiconductor sources available to us, which are JPL's custom-designed and fabricated GaAs Schottky diode frequency-doublers configured in a four-way power combining waveguide [21] and pumped with a multi-Watt W-band power amplifier using GaN chips obtained from Raytheon Corporation [22]. Figure 2 shows measurements of G-band power achieved in VIPR, both at the doubler's output flange and following a calibration-loop coupler and a 90° waveguide bend (see inset sketch) which combined introduce ~2 dB of loss for a transmit power of ~200 mW. This transmitter configuration was used for the ground measurements presented in Figures 3, 5, and 9. Since then, for airborne deployment (Figure 10) an updated hardware configuration uses a low-loss coupler (Section IIIE), no 90° bend, and higher pumping power at W-band. With these changes, VIPR's transmit power is closer to 300 mW.

VIPR's receiver, meanwhile, consists of an InP low noise amplifier (LNA) [23] and a G-band subharmonic GaAs Schottky diode mixer, both designed at JPL. Noise temperature measurements of the complete VIPR receiver were made using the Y-factor hot/cold-load technique with the loads positioned in front of the receiver beam horn. The VIPR system noise figure over 167-174.8 GHz is around 9-10 dB. With the improved lower-loss calibration-path coupler and also a

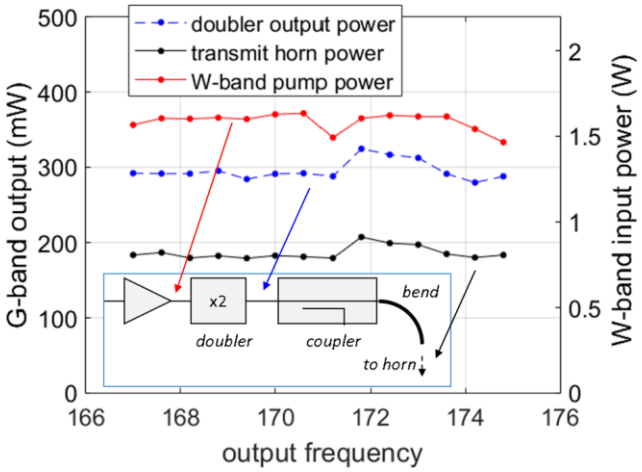

Figure 2. Measured powers at different points in the transmit chain leading to nearly 200 mW of transmit power at 167 and 174.8 GHz.

different LNA chip, the system noise figure (excluding losses through the optics) improved by about 1.8 dB to average 7.8 dB over the VIPR band. Except for Figure 10, the radar measurements presented in this paper use the lossier calibration path couplers (i.e., the worse noise figure).

The last high-level radar design parameters that drive VIPR's sensitivity are its detection bandwidth and averaging methodology. Because the radar's GaN power amplifiers and GaAs Schottky diodes are capable of continuous-wave operation without damaging the instrument's receiver, VIPR uses FMCW pulse modulation to maximize its sensitivity. While FMCW radar is uncommon in lower frequency radars where higher-power sources are readily available, it is a favored approach in short-range, high-frequency, low-power radar systems such as automotive navigation radar. FMCW radar architectures very similar to VIPR have also been used by our group for more than a decade in other high-frequency radar systems spanning 95 to 700 GHz [24].

VIPR uses a bidirectional and continuous linear-frequency-chirped waveform. Bidirectional chirps have a primary benefit of allowing the receiver floor to be continuously "exposed" and subtracted from the cloud and rain targets obtained as shown in [16]. The radar's typical chirp period and bandwidth is 1 ms and 10 MHz, corresponding to a final detection bandwidth of 1 kHz (inverse of the chirp time) and a range resolution of 15 m. Choosing longer chirp times can result in higher single-pulse SNR through coherent averaging as long as the Doppler bandwidth of the ensemble of radar targets (i.e., the inverse of the coherence time of the echo signal itself) is narrower that the detection bandwidth. For VIPR mounted in an aircraft moving at a typical speed of $v = 80$ m/s, the Doppler bandwidth from the platform motion and the radar's finite beam width will be around $\Delta f_{dop} \approx 2v/D = 355$ Hz [25], where $D = 44$ cm is the radar's effective aperture diameter after accounting for illumination taper. This is somewhat below the current 1 kHz detection bandwidth, so that another factor of ~3 in single-pulse SNR improvement can be realized in static cloudy volumes.

Table I summarizes the major radar system parameters that can be used to calculate VIPR's sensitivity. The quantity

dBZ_{min} characterizes the performance of cloud and precipitation radars, most commonly for lower frequencies operating in the Rayleigh regime. It represents the attenuation-free, small-hydrometer volumetric reflectivity factor that gives an SNR of unity (0 dB) for VIPR's 1 kHz single-pulse detection bandwidth and 15 m range resolution.

Table I: VIPR's radar parameters for the data of Figures 3, 5, and 9.

VIPR Radar Parameter	Value
Radar frequency	167-174.8 GHz
Transmit power	180-210 mW
Antenna gain	58 dB
Noise figure	10 dB
Range resolution	15 m
Detection noise bandwidth	1 kHz
single-chirp dBZ_{min} at 1 km range	-40 dBZ

Using 200 mW for the transmit power and the other hardware parameters from Table I, a scattering dielectric constant factor of $K^2 = 0.6$, and ignoring propagation attenuation, we find VIPR capable of detecting dBZ_{min} = -40 dBZ scatterers for a single chirp waveform from 1 km ranges. This makes VIPR an exquisitely sensitive cloud radar at short ranges when attenuation due to propagation is negligible, comparable to other state-of-the-art airborne systems (e.g., [26]).

C. VIPR Calibration with a Spherical Target

As a validation of VIPR's sensitivity, we calibrated the radar using a 2-inch-diameter metal sphere suspended by fishing line in clear air at a horizontal distance of about 500 m, shown in Figure 3. VIPR was carefully pointed by hand so that the sphere lay along its boresight. Using local measurements of the ground-level temperature (16 C), pressure (975 mbar), and water vapor density (5 g/m^3), the two-way atmospheric attenuation at 167 GHz is estimated to be 1.2 dB based on the atmospheric propagation models from [20]. The standard radar equation [27], using the parameters of Table I, predicts a single-pulse SNR of 48.6 dB.

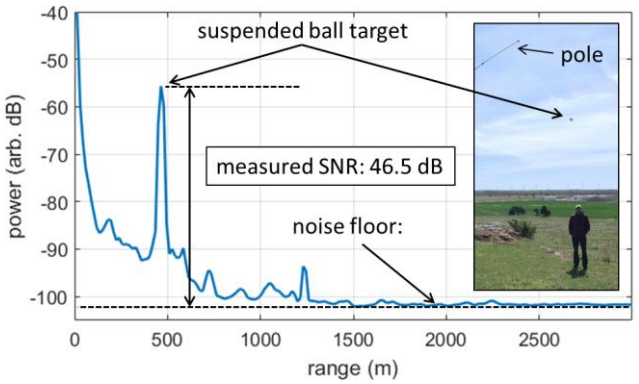

Figure 3. Radar range spectrum with the beam aligned to a two-inch-diameter spherical ball target at ~500 m range. The photograph shows the measurement geometry with a ball target suspended above ground level.

The detected single-pulse baseband spectrum in Figure 3 reveals a measured SNR of 46.5 ± 0.5 dB, calculated by integrating the resolved peak power lobe from the target. This is about 2 dB less than the calculated estimate, possibly because of drifts or inaccurate knowledge of the radar's hardware parameters (transmit power, receiver noise, antenna gain), imperfect knowledge of the water vapor absorption all along the beam path to the target, off-boresight target positioning, scattering effects of the suspending nylon thread, and beam spillover in the focusing optics.

III. VIPR's RF, Digital, and Optics Design

A. RF/Digital Block Diagram

A simplified block diagram of VIPR's RF and digital electronics is shown in Figure 4. The design is based on the FMCW radar architecture of JPL's 340 and 680 GHz radars [28]. The transmitter and receiver chains are driven at offset frequencies for heterodyne detection over 167-174.8 GHz. The two chains begin with two Ka-band synthesizers offset by 150 MHz. The synthesizers are selected for their excellent phase noise performance (about -112 dBc/Hz at 100 kHz offset) as well as sufficiently fast switching speeds (1 ms). Fast switching is important for VIPR to capture differential measurements before the scene reflectivity changes significantly. Synthesizer tuning was also valuable for testing differential absorption measurements at different frequencies within the 167-174.8 GHz operating band.

The synthesizer signals are frequency-tripled using high-efficiency JPL-made Schottky diode W-band triplers [21], followed by single sideband up-conversion at W-band of chirp waveforms centered at 8 GHz. The digitally generated chirps typically span 10 MHz, but are programmable up to much higher bandwidth. They are also phase-locked and frequency-offset from each other by 2.5 MHz in order to offset zero-range radar signals from zero frequency in base-band.

Following the chirp up-conversion, the transmit-chain signal is amplified and frequency-doubled, then passed through a directional coupler for loop-back calibration, and out a beam horn to the system feed optics. On the receive path, the chirping W-band local oscillator (LO) pumps a subharmonic double-sideband mixer fronted by an InP LNA. This is where the deramping stage of the FMCW range compression occurs. The LNA is also weakly coupled to the calibration path between the LNA and the receive beam horn. The calibration path has a G-band InP RF switch designed at JPL and fabricated by Northrup Grumman Corp. using an InP process (see Section IIIC).

A notable aspect of VIPR's design is the way in which the IF signal emerging from the G-band front-end mixer is down-converted to baseband. This IF signal contains the reflectivity profiles encoded as spectral content. It is centered at 905 MHz, which comes from a difference of the sextupling of the original Ka-band synthesizer outputs, plus a doubling of the two chirper's offset frequencies, so that 150×6 + 2.5×2 = 905 MHz. The IF signal is de-modulated in an I/Q mixer pumped with a 900 MHz local oscillator that itself emerges from the mixing of the frequency-tripled synthesizers (for a 450 MHz IF), followed by a frequency-doubling circuit. The 5 MHz IF signal from the base-band I/Q mixer is amplified, filtered for anti-aliasing, and digitally sampled. Shifting zero-range signals by 5 MHz from DC assists in accurate calibration. In the final base-band

spectrum computed using a digital Fast Fourier Transform (FFT), cloud and precipitation signals are shifted from a 5 MHz center frequency by the standard FMCW radar factor of $f_{IF} = 2KR/c$ where K is the chirp rate, R is the target range, and c is the speed of light. For a typical chirp time and bandwidth of 1 ms and 10 MHz, the proportionality between frequency and range is 67 kHz/km.

B. *Phase Noise Cancellation and T/R Isolation*

The method of using the product of the transmit and receive chains' source signals as a local oscillator to down-convert FMCW echoes is identical to the architectures we have used in other high-frequency radar systems such as [3, 28]. It ensures that the phase noise of the local oscillator for the I/Q mixer (green path in Figure 4) is highly correlated with the phase noise of the transmitted 170 GHz signal that leaks directly into the receiver port (blue path in Figure 4). Similar correlation exists for phase noise originating in the receiver chains source oscillator. The T/R leakage signal, despite being minimized by an optical feed design with more than 80 dB of isolation, is typically the dominant signal detected by the radar. The leakage signal carries with it a broadband phase noise skirt which can overwhelm the receiver's thermal noise. Thus without phase noise cancellation that occurs within the I/Q mixer, VIPR would not be thermal-noise-limited by the front-end LNA.

To demonstrate this, Figure 5 shows three radar spectra obtained with VIPR pointing into a clear sky. Each is the average of 2000 pulses with the radar tuned to 167 GHz with standard parameters of a 10 MHz chirp bandwidth and 1 ms chirp time. The blue trace is obtained when the transmitter power is turned off, and it exhibits a flat noise floor at a level of -135 dBm per 1 kHz Fourier bin. When the transmitter is turned on, the red curve is obtained, showing the zero-range T/R leakage signal with a peak magnitude of -62 dBm. With a 1.8 dB correction for a Hann window used in the power spectrum calculation, and given a 167 GHz transmit power of approximately +23 dBm from Figure 2, the T/R isolation is estimated to be 83 dB. This remarkably high value of isolation is a consequence of the radar's optical design described below in Section IIIE.

The inset to Fig. 5 shows that turning on the transmit power increases the noise level by only ~0.25 dB at 6 km range (a 400 kHz offset in IF frequency). This excellent performance is a consequence of two factors: 1) high T/R isolation, and *2)* phase noise cancellation in the I/Q mixer. To show the importance of effect #2, the black curve in Figure 5 was obtained under identical conditions as the red curve, but with a 450 MHz signal leading to the I/Q mixer generated with an *external* synthesizer whose phase noise is uncorrelated with the internal VIPR synthesizers. For this situation, the noise floor at distant ranges is approximately 15 dB higher than the thermal-limited value. Therefore, Figure 5 demonstrates how VIPR's nearly-thermal-limited sensitivity is only achieved when its IF down-conversion to baseband utilizes a local oscillator derived from the original transmit and receive chains' sources. In theory, if the group delays of the blue and green paths were identical, then the phase noise cancellation would be perfect, and no special effort would be needed to achieve very high T/R isolation. However, some delay imbalance is inevitable in practice for two reasons. First, the RF hardware's physical dimensions and, especially, group delay from filters can cause significant delay imbalance. In Figure 4, this consideration motivated the use of

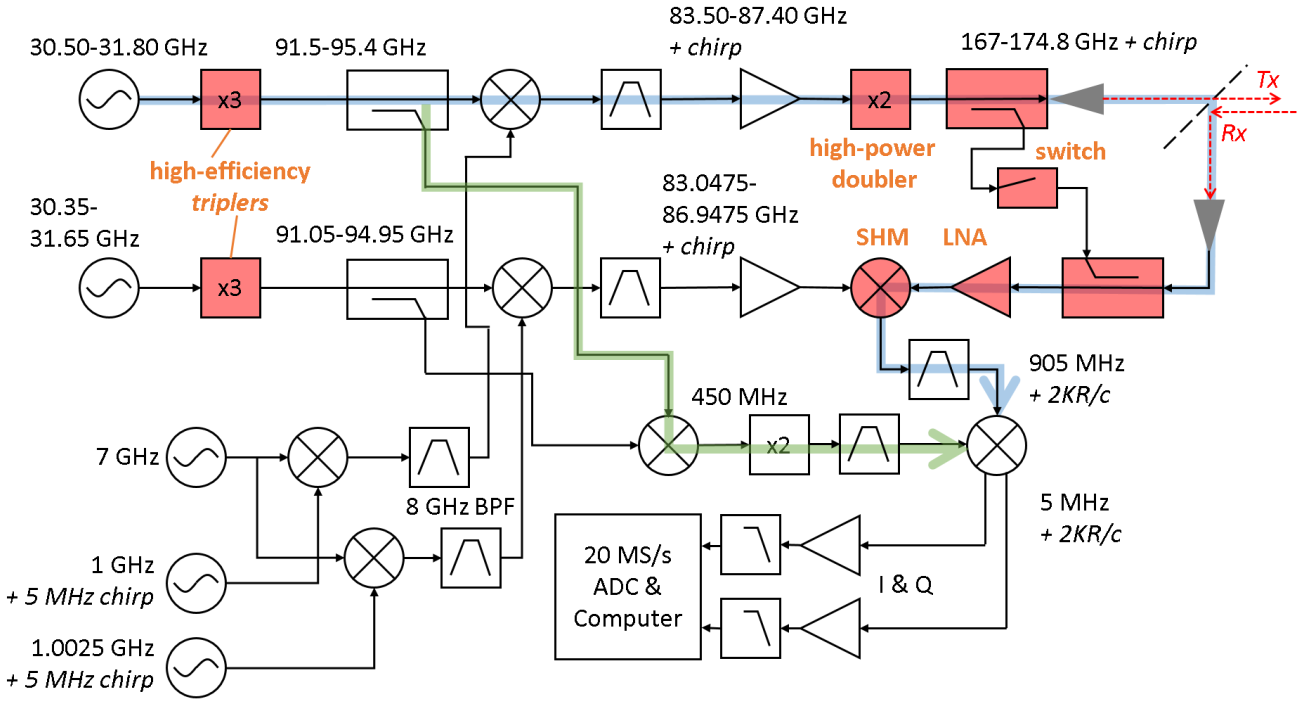

Figure 4. VIPR's block diagram. The red-shaded components were custom-developed by JPL. The paths indicated by the thick blue and green arrows represent the transmitter leakage path and a reference path. When the paths have well balanced electrical lengths, a high degree of synthesizer phase noise cancellation occurs in the 900 MHz I/Q mixer that down-converts to baseband.

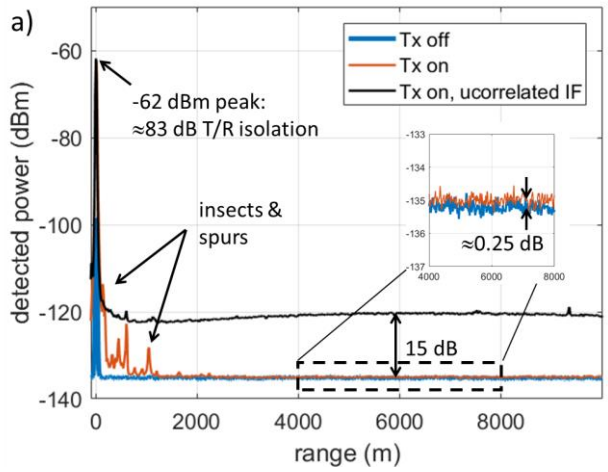

Figure 5: VIPR's detection noise floor is virtually unaffected when the transmitter is turned on (blue vs red curves, and inset). However, if the phase-noise-cancellation reference path in Fig. 6 is not used (black), the noise floor greatly increases because of strong near-zero-range transmit/receive leakage.

a pair of identical band-pass filters on the 900 MHz sections of the green and blue paths, each with ~5 ns of group delay (1.5 meters in free-space).

Second, the delay in the blue path can be significant, depending on the specific path taken by the free-space beam that couples T to R. For VIPR, based on its sensitivity to the placement of RF absorbing foam, we estimate that beam spillover around the primary antenna is the main source of T/R leakage, corresponding to a several-meter delay imbalance. This estimate is consistent with the observed 0.25 dB noise floor increase in Figure 5, which would result from an additive phase noise level of about $10\log_{10}(1\text{-}10^{-0.025})$ = -12.5 dB below the thermal noise floor. Referenced to the 15 dB excess in phase noise level when an uncorrelated source is used (Figure 5), this gives an estimated F = 12.5 + 15 = 27.5 dB phase noise suppression due to balancing the path delay. Then using the formula from [29] relating the phase noise modulation factor to a path delay of τ for an offset frequency of f_m = 400 kHz,

$$F = 4 \cdot \sin^2(2\pi f_m \tau/2) = 2 - 2\cos(2\pi f_m \tau), \quad (1)$$

the path-delay imbalance consistent with Figure 5 is 17 ns, or a 5 m free-space path. That distance is consistent with the suspected source of T/R coupling via beam spillover reflecting off the structure surrounding the primary antenna.

C. Calibration Path

VIPR's primary measurement objective, retrieving humidity profiles inside clouds and precipitation, requires no calibration of transmit power or receiver gain because drifts of those variables are common-mode terms that drop out when comparing echo power at two different ranges and two different frequencies. Nonetheless, VIPR includes a calibration loop to facilitate two secondary measurement objectives: absolute cloud/precipitation reflectivity and clear-air partial water vapor (PWV) column. For absolute calibration, VIPR would first acquire a spherical-target reflection similar to that of Figure 3, and then scale subsequent measurements based on drifts in the calibration-loop signal.

It is tempting to implement a calibration loop based only on the -83 dB transmit/receive coupling that is inevitable from the VIPR optics design. However, we are reluctant to rely on this stray leakage as an accurate calibration method because it can potentially change based on what objects are placed in the vicinity of the VIPR hardware that can cause very low-level coupling. Therefore, VIPR's dedicated calibration loop consists of two -30 dB directional couplers and a G-band electronic switch, as shown in the block diagram of Figure 4. The switch periodically couples a small portion of the radar's RF signal to pass directly from the transmit path to the receiver's LNA, so that source power and gain drifts can be monitored.

VIPR's G-band switch was originally developed for radiometric calibration applications, and was designed by JPL and fabricated by Northrop Grumman Corp. using 75-µm thick InP MMIC PIN process. This MMIC switch was implemented using coplanar waveguide (CPW) technology and utilizes PIN diodes as switching elements for low loss and fast switching speed [30].

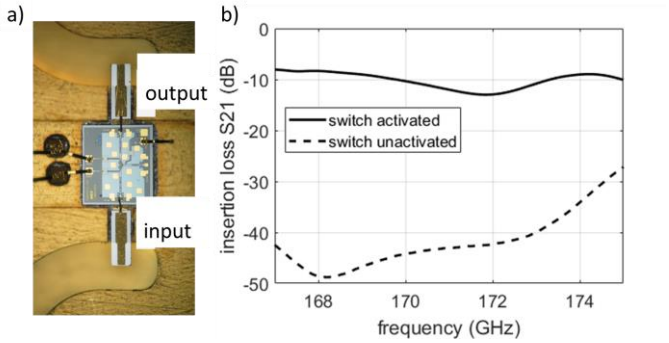

Figure 6. JPL's a) Photograph of G-band switch mounted in a waveguide block. b) The main performance criteria of the switch is that it has a large insertion loss contrast between its activated and deactivated states, and 15-40 dB contrast is measured over the VIPR band.

To achieve a maximum on/off insertion loss ratio for VIPR, the chip was packaged in a SPST (Single Pull Single Throw) configuration. Mounted in a waveguide block, the switch is shown in Figure 6a. Vector Network Analyzer (VNA) measurements of Figure 6b show that its on/off insertion loss ratio is between 32 and 13 dB over the VIPR band, with an insertion loss of about 9 dB when the switch is activated for RF signal to pass. Together with losses through the two couplers and a few inches of WR5 waveguide, the switch's on/off ratio is sufficient to accomplish two objectives: 1) when the switch is not activated, the RF signal passing through the switch is much smaller than the native T/R quasioptical leakage, and hence has no significant effect on VIPR's sensitivity; and 2) when the switch is activated, the zero-range signal of the RF power passing through the switch dominates over the native quasioptical leakage, thus providing a stable radar calibration path insensitive to small, incidental changes leakage levels.

VNA measurements have also confirmed that the switch itself is not very susceptible to temperature changes, with a typical insertion loss drift of only 0.03 dB/°C from 4° to 34° C. This implies that <1 dB of calibration accuracy will be

achievable as long as the switch's temperature is stable to within about ±15° C.

While calibration during operation is valuable, it comes at a significant performance cost to VIPR because losses through the transmit and receive couplers are significant at G-band. For example, Figure 7a (dashed black) shows VNA-measured insertion loss and coupled power through commercially procured, 5.6 cm long, G-band -30 dB couplers. Having 1.6 dB insertion loss each, these together degrade VIPR's sensitivity by approximately 3.2 dB compared to not having any couplers for the calibration path. The measurements and humidity retrievals reported in [17], as well as the radar measurements in this paper, with the exception of those in Figure 10, were obtained with these relative high-loss components in place.

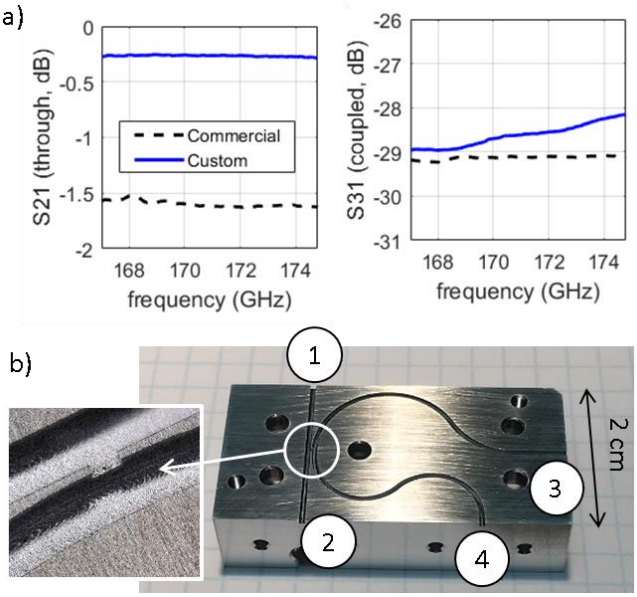

Figure 7: a) JPL-designed -30 dB 170 GHz couplers have been fabricated that are much less lossy than commercially available full-band couplers. b) The couplers feature a single iris and a very short through-path length.

Given significant room for improvement, we subsequently designed and fabricated custom couplers with a much smaller through-port waveguide length. The design and optimization of the couplers was achieved using a full-wave electromagnetic simulation software, CST Microwave Studio. The coupler geometry is shown in Figure 7b, and it consists of a single-iris (inset) four-port waveguide structure with -30 dB coupled Ports (1,3) and (2,4). Figure 7a shows its S_{21} and S_{31} measurements. Only 2.0 cm long now, the insertion loss of these couplers was measured to be about 0.27 dB, a 1.3 dB improvement over the commercial version. A tradeoff to reach this performance is that these couplers are narrower band than the commercial full-band couplers, although their bandwidth is still sufficient for VIPR. Together with the elimination of a lossy (0.4 dB) WR5 waveguide bend that had previously been needed for the old coupler to mate with the VIPR horn geometry, this results in a total improvement in sensitivity (dBZ_{min}) of ~3 dB.

D. Digital Signal Processing

The baseband radar signal prior to digitization consists of a 5 MHz tone, arising from either direct T/R leakage or the open-switch calibration loop, plus signals from distant targets at frequency offsets (from 5 MHz) proportional to their range with a typical scaling of 67 kHz/km. Digitization is done at a sampling rate of 20 MS/s with a 14-bit analog-to-digital converter (ADC), and for a 1 ms duration chirp, a pulse-to-pulse dead time of 10 μs is needed for software triggering of the chirp synthesizers.

Several techniques are employed in order to realize a high-duty-cycle mode of radar operation with real-time signal processing and data compression, visualization, and archiving. First, due to the finite (~1 ms) switching time of the Ka-band synthesizers, 10 total chirps (i.e., 5 up and 5 down) are performed at a given frequency before triggering the synthesizers to switch and subsequently waiting for 1.3 ms before the next chirp initiation. This establishes a maximum possible duty cycle of 88%. Second, radar signal processing (described below) is performed on a set of 400 previously acquired pulses in parallel with acquisition of the current set. The resulting system duty cycle including all data display and saving to permanent memory is 83%.

Given a set of previously acquired chirp signals, the signal processing procedure is to apply a Hann window to the complex I/Q baseband time-domain signal, and then compute a two-sided power spectrum using the fast Fourier transform. These spectra are then averaged and saved as typically 1000-pulse averages for the final up- and down-chirp power spectra.

E. Optics Design

Single-antenna FMCW radars with appreciable transmit power are uncommon because, with the transmitter always active during the entire detection (chirp) interval, T/R leakage through conventional waveguide circulators can introduce significant phase noise as in Section IIIB, or saturate or even burn out the receiver's LNA. Geometries with separate transmit and receive primary antennas are therefore often preferred for FMCW radar because separating the transmit and receive antennas ensures very low leakage levels.

In contrast, VIPR uses a quasioptical T/R duplexing method that achieves extremely high isolation while still using a single primary antenna. This reduces the instrument size and cost compared to a dual-antenna configuration, which is especially valuable for deployment on airborne platforms with fixed aperture constraints. VIPR separates the transmit and receive signals using a quasioptical circular polarization duplexer whose main elements are a polarization-separating wire grid and a linear-to-circular grating polarizer to transmit and receive circular polarization using two orthogonal linearly polarized beam horns. The method is essentially identical, except for a frequency-scaling and a different beam-path geometry, to the one we developed first for a 680 GHz radar [31] and subsequently for an earlier breadboard version of VIPR [15].

The final VIPR optics configuration is shown in the model of Figure 8a, along with a photograph of the VIPR optics in Figure 8b. A challenge in achieving these very high isolations, which are needed to ensure that VIPR's receiver is very nearly thermal-noise-limited as in Figure 5, is that beam spillover around the radar's feed optics and primary aperture can lead to

excessive near-field leakage. We experimentally found that a conservative -30 dB taper on the primary aperture, with a 57.8 dB antenna system gain, is needed to keep the T/R leakage low enough for thermal-noise-limited detection. While this edge taper for the VIPR primary ensures that stray radiation is minimized, it also means that the aperture efficiency is quite low for a reflector antenna. Physical Optics simulations indicate that roughly 30% of VIPR's effective aperture area is lost when operating with a -30 dB taper compared to a more conventional -12 dB taper. This partly undermines our original motivation of saving mass and volume by building a single-antenna radar, since a radar design with separate antennas for the transmitter and receiver, and equivalent sensitivity, could likely use a more aggressive edge taper while not requiring double the total area as VIPR's single 60 cm diameter antenna.

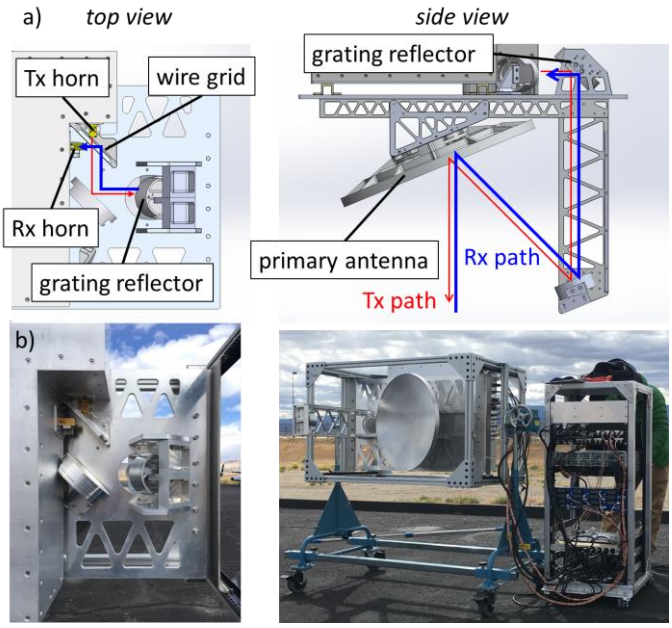

Figure 8: a) A beam-path layout showing VIPR's quasioptical grid, grating, and reflector layout. b) A photograph of VIPR showing the duplexing section (left) and the entire radar assembly (right) mounted on a rotation platform. Unusual for Watt-scale FMCW radars, VIPR uses a single-antenna configuration.

IV. Cloud and Humidity Measurements Example

For ground-testing, VIPR was mounted on a rotation stage (Figure 8b) so that it can be pointed at any elevation angle. The cloud and rain data shown in Figure 9 were obtained on April 13, 2019, beginning at 15:15 UTC, at the SGP-ARM research facility in Oklahoma. Further environmental information about this data, and VIPR's primary results from the campaign, are summarized in [17].

The cloud curtain of Figure 9a were obtained with VIPR pointed in the zenith direction, transmitting at 167 GHz, and using 1 ms chirp times with a 10 MHz bandwidth (15 m range resolution). The cloud profile changes over time as the storm passes overhead, showing an approximate representation of the cross-sectional cloud curtain over miles in horizontal scale despite VIPR being stationary. Noticeable rain began to hit the ground toward the end of the nearly 3-hour measurement, at which time this observation was ended and VIPR rolled indoors. The cloud and rain curtain data in Figure 9a have been converted to an effective cloud reflectivity dBZe according to the definition in [27], based on the spherical-target radar calibration of Figure 3. Thin horizontal lines below 2 km (also visible as spikes in Fig. 9b) are spurious artifacts from the VIPR frequency-generation electronics. This is the same data set presented in Figure 3 of [17], but with a format here that shows the noise floor and some additional detail. For example, the higher intensity scattering near 1.8 km altitude, which might be from rainfall that evaporates before reaching the ground, appears to be the cause of higher phase noise rising above the radar's thermal noise floor above 8 km. Vertical transient streaks showing regions of weaker signals at higher but not lower altitudes are also visible, for example near 4000 s and 8000 s, may be caused by regions of temporarily higher attenuation at lower altitudes.

In Figure 9b, vertical range-profiles of detected power are shown for both 167 GHz (blue) and 174.8 GHz (red) signals. These profiles were obtained by averaging the first 10 minutes of the data set, denoted by the rectangular region enclosed in the black dashed box in Figure 9a. Each curve is normalized to 0 dB at 120 m altitude. In this way, it can be readily seen how the 174.8 GHz signal is more strongly attenuated with altitude than the 167 GHz signal. The black curve in Figure 9b is the difference between the two signals. The slope of this difference signal is the measured dB/km rate of change in the differential absorption between the two frequencies. This is the sought-after quantity to retrieve range-resolved humidity. The slope can be seen to start off steeper, and then gradually become more shallow. This means that at lower altitudes there is more differential absorption from the expected higher absolute humidity than at higher altitudes.

Quantitatively, as described in [16], this slope can be mapped into an estimate of the absolute humidity as a function of height. This is shown in the blue curve of Figure 9c, where the retrieved water vapor density in g/m^3 is plotted along with a "truth" value (black dashed curve) obtained from a balloon-borne radiosonde launched very near the beginning ($t = 0$ s) of the data set in Figure 9a, from a location approximately 500 m away from the radar location. The agreement between VIPR's profile and the radiosonde data is excellent, with maximum deviation of only ~0.5 g/m^3. In [17], more comprehensive comparisons are presented between retrieved humidity and in-situ radiosonde measurements, and typical errors are in the 0.5-1 g/m^3 range. These uncertainties are dominated by systematic biases introduced by what we believe are spatial gradients in the hydrometer drop-size-distribution.

In late 2019 and early 2020, VIPR was operated from a nadir-viewing airborne platform for initial assessment of its performance. Data analysis to extract and validate inside-cloud humidity profiles and other physical parameters is an ongoing task that will be presented in future work. However, the effort revealed an important measurement concern that is presented here. In Figure 10, two 200-pulse-averaged 167 GHz radar spectra (chirp-up only) are shown for VIPR flying at a 2.7 km altitude over the ocean off the coast of Santa Barbara County, California on November 14, 2019 at about 19:00 UTC. The

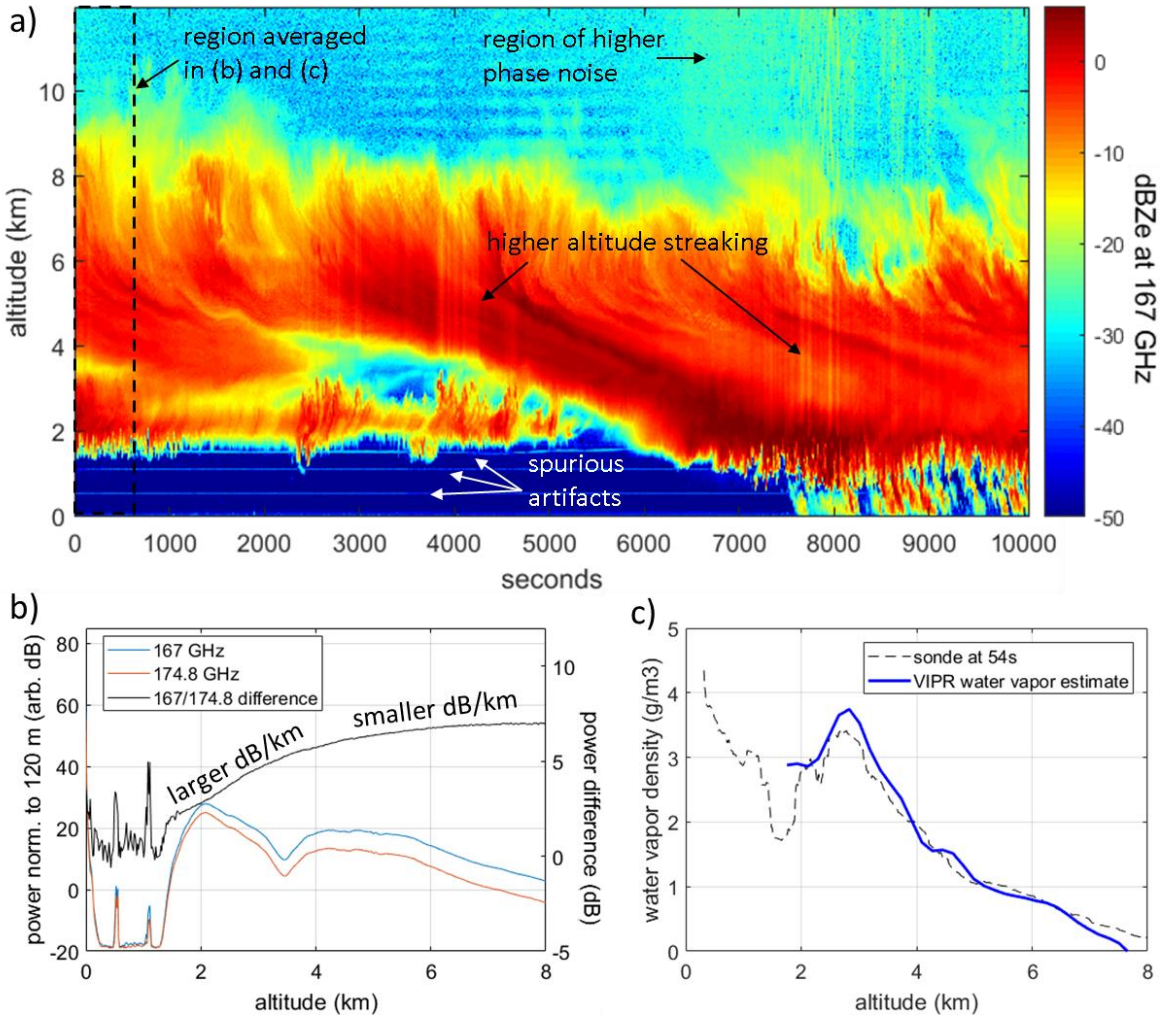

Figure 9. a) A nearly 3-hour cloud curtain obtained by VIPR pointed in the zenith direction during testing at the SGP-ARM facility. Cloud reflections up to 10 km in altitude are observed. The color scale units are in dBZ. b) Time-averaged range-profiles of the cloud over the first 10 minutes of the measurement (dashed black box in (a)) for 167 and 174.8 GHz. The steeper differential signal at lower altitudes, compared to higher altitudes, is a sign of higher humidity near ground level. c) A quantitative humidity profile for the time-averaged data of (b), using the algorithm of [17] shows excellent agreement with a coincident radiosonde measurement.

skies had thin, broken low clouds at the time. The blue radar spectrum is for the airplane flying level with a beam-ocean incidence angle of 2°, while the red spectrum is for a banking angle of 19°.

The blue near-nadir trace shows a very bright ocean reflection at about 2.7 km in range. Using a ground calibration measurement at 167 GHz and accounting for 7 dB of two-way attenuation to the surface, an estimate based on a nearby National Weather Service radiosonde launch, the native surface backscattering coefficient for this near-nadir measurement is $\sigma_0 \approx 15$ dB. The surface signal is nearly as strong as the native T/R radar leakage signal at zero range. Unlike the latter, however, the surface signal does not exhibit strong phase noise suppression over the whole radar bandwidth due to the mixing of highly correlated signals in the I/Q mixer of Figure 4, as described in Section IIIB. Instead, the phase noise modulation factor of Eq. 1 generates the strong sinusoidal range-sidelobes visible in the blue curve of Figure 10, reaching levels more than 20 dB above the thermal noise floor.

The consistency of Eq. 1 can in fact be confirmed by calculating the expected phase noise lobes based on an independent measurement of VIPR's Ka-band transmitter synthesizer. Labeling the synthesizer's measured phase noise $\mathcal{L}_0(f_m)$ (not shown here) in units of dBc/Hz as a function of offset frequency f_m, the predicted phase noise level for the measurement scenario of Figure 10 is:

$$\mathcal{L}_{predict}(f_m) = \mathcal{L}_0(f_m) + 20\log_{10} 6 + F[\text{dB}] \qquad (2)$$

where the offset of $20\log_{10} 6$ comes from the frequency-multiplication factor of six to reach G-band and the last offset F comes from the delay-correlation factor of Eq. 1 where a one-way target range of 2657 m ($\tau = 17.7$ µs round trip) was used based on the measured range of the bright ocean-surface target. The phase noise $\mathcal{L}_0(f_m)$ was measured using the 450 MHz IF signal indicated in the green reference path in Fig. 4, with a correction of $20\log_{10} 3$ for the frequency-tripling prior to mixing down to 450 MHz, and of $20\log_{10} 2$ for the doubled

noise contribution of the two identical synthesizers. Finally, by adding 30 dB to Eq. 2 for the 1 kHz detection resolution for Figure 10, and also using the frequency-to-range conversion factor of 400 kHz/km appropriate for this data set

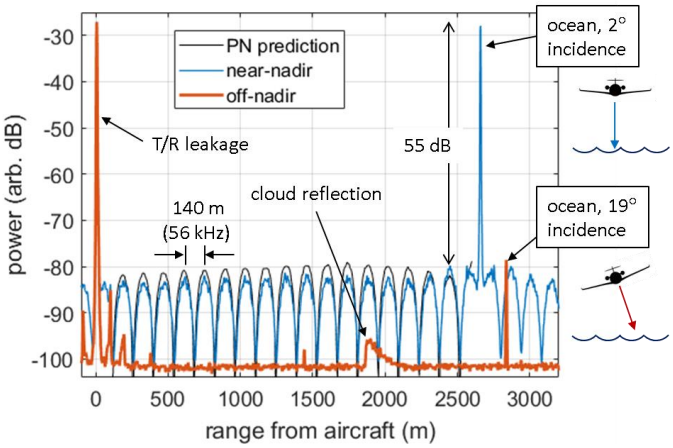

Figure 10. Deploying VIPR in an aircraft above the ocean reveals a very bright specular reflection from the surface when the beam points in the near-nadir direction (blue trace), accompanied by strong phase noise sidelobes. Pointing off-nadir by 19° (red trace) reduces the ocean-reflection magnitude so the phase noise sidelobes are below the instrument noise floor, revealing a low-altitude cloud.

where a 60 MHz chirp bandwidth was used, we obtain the black trace in Figure 10. The agreement with the near-nadir measurement (blue) is good, with a maximum discrepancy of 2.5 dB around 1800 m. We speculate, without confirmation yet, that this discrepancy might be from the synthesizers exhibiting somewhat different phase noise characteristics when operating at the lower temperatures in the aircraft.

Clearly the strong range sidelobes from surface reflections would be a major obstacle for over-ocean VIPR deployment if there were no way to mitigate them. One strategy could be to use lower phase noise source oscillators, but superior room-temperature microwave electronic sources with more than 20 dB phase noise improvement do not exist. A second way that strong range sidelobes are suppressed comes naturally to VIPR's concept of operation: when sufficiently thick clouds or near-surface rain is present, the apparent reflectivity of the ground is very often attenuated enough that the phase noise lobes are not a problem.

A third approach for reducing phase-noise sidelobes is to point the radar off-nadir, which is done for the red trace in Figure 10. That data is taken within two minutes of the blue curve, after the aircraft has banked by 19° in a turn. With the ocean reflection no longer at near-normal incidence, the surface reflection intensity is reduced by many orders of magnitude (and shifted farther in range from the different beam path angle), pushing the phase noise range side-lobes below the instrument's thermal noise level. As a result, the red trace in Figure 10 reveals a weakly scattering cloud at a range of ~2 km, i.e., within 1 km of the ocean surface. This low-cloud detection would have been otherwise impossible to detect in the radar spectrum taken with near-nadir pointing.

In future data analysis, we will use VIPR's airborne measurements to quantitatively map how the instrument's sensitivity to low-altitude clouds depends on the surface scattering characteristics, how both ocean and land backscattering coefficients vary as a function of incidence angle, and how they depend on the amount of intervening vapor and cloud-hydrometeor attenuation. Part of this assessment must consider the effect of VIPR's finite beam size, especially for off-nadir pointing, because illuminating a wide ground swath over multiple range bins will complicate the phase noise response when the strong echo tone is not a point-like scatterer confined to a single range bin.

I. Conclusions

Despite very low peak transmit powers compared to conventional kW-level pulsed cloud radars, VIPR exhibits great sensitivity to clouds, and its frequency tunability enables a new DAR measurement method to obtain humidity profiles. Airborne testing has begun, which will allow inside-cloud water vapor sounding measurements to be made from above the clouds, so that wider geographic areas and more variations in cloud characteristics can be measured. The impact of ground or sea clutter on the instrument's sensitivity is an important to consideration for observing clouds from above, and will be relevant to a future orbital version of VIPR. Such a scenario will also require a reassessment of how to generate sufficiently high levels of G-band power for remote sensing of clouds from distances of hundreds of kilometers. Nonetheless, as a ground- or airborne-based cloud radar system that uses innovative design approaches and state-of-the-art millimeter-wave components, VIPR has already demonstrated a new measurement approach that can be widely applied to earth science.

Acknowledgment

We thank Douglas Dawson and Pekka Kangaslahti of JPL for the use of the G-band switch and advice on packaging. We also acknowledge Steve Dinardo, Simone Tanelli, and Stephen Durden of JPL for guidance on topics of cloud radar architectures and measurements.

References

[1] A. Battaglia, C.D. Westbrook, S. Kneifel, P. Kollias, N. Humpage, U. Lohnert, J. Tyynela, and G.W. Petty, "G band atmospheric radars: new frontiers in cloud physics," *Atmospheric Measurement Techniques*, vol. 7, pp. 1527-1546, 2014.

[2] R. Appleby and H.B. Wallace, "Standoff detection of weapons and contraband in the 100 GHz to 1 THz region," *IEEE Transactions on Antennas and Propagation* vol. 55, no. 11, pp. 2944-2956, 2007.

[3] K.B. Cooper, R. J. Dengler, N. Llombart, B. Thomas, G. Chattopadhyay, and P. H. Siegel, "THz imaging radar for standoff personnel screening," *IEEE Transactions on Terahertz Science and Technology*, vol. 1, pp. 169-182, 2011.

[4] W.R. Deal, T. Foster, M.B. Wong, M. Dion, K. Leong, X.B. Mei, A. Zamora, G. Altvater, K. Kanemori, L. Christen, and J.C. Tucek, "A 666 GHz demonstration crosslink with 9.5 Gbps data rate," *2017 IEEE MTT-S International Microwave Symposium*, pp. 233-235, 2017.

[5] F.T. Ulaby, et al., *Microwave radar and radiometric remote sensing*, Ann Arbor, Michigan: University of Michigan Press, 2014. pp. 353-356.

[6] A. Tang, Y. Kim, T. Reck, Y. Tang, Y. Xu, G. Chattopadhyay, B. Drouin, I. Mehdi, and F. Chang, "A 177–205 GHz 249 mW CMOS-based integer-N frequency synthesizer module for planetary

exploration," *IEEE Transactions on Terahertz Science and Technology* vol. 8, no. 2, pp. 251-254, 2018.
[7] Y. Kim, Y. Zhang, T.J. Reck, D.J. Nemchick, G. Chattopadhyay, B. Drouin, M.F. Chang, and A. Tang, "A 183-GHz InP/CMOS-Hybrid Heterodyne-Spectrometer for Spaceborne Atmospheric Remote Sensing," *IEEE Transactions on Terahertz Science and Technology*, vol. 9, no. 3, pp. 313-334 (2019).
[8] P. Hillger, J. Grzyb, R. Jain, and U. Pfeiffer, "Terahertz imaging and sensing applications with silicon-based technologies," *IEEE Transactions on Terahertz Science and Technology* vol. 9, no. 1, pp. 1-19, 2018.
[9] Z. Griffith, M. Urteaga, and P. Rowell, "180–265 GHz, 17–24 dBm output power broadband, high-gain power amplifiers in InP HBT," *2017 IEEE MTT-S International Microwave Symposium*, pp. 973-976, 2017.
[10] W.R. Deal, K. Leong, A. Zamora, V. Radisic, and X. B. Mei, "Recent progress in scaling InP HEMT TMIC technology to 850 GHz," *2014 IEEE MTT-S International Microwave Symposium*, pp. 1-3, 2014.
[11] B. Schoch, A. Tessmann, A. Leuther, S. Wagner, and I. Kallfass, "300 GHz broadband power amplifier with 508 GHz gain-bandwidth product and 8 dBm output power," *2019 IEEE MTT-S International Microwave Symposium*, pp. 1249-1252, 2019.
[12] S.H. Kim, R. Fan, and F. Dominski, "ViSAR: A 235 GHz radar for airborne applications," *2018 IEEE Radar Conference*, pp. 1549-1554, 2018.
[13] R.M. Narayanan, C.C. Borel, and R.E. McIntosh, "Radar backscatter characteristics of trees at 215 GHz," *IEEE transactions on Geoscience and Remote Sensing*, vol. 26, no. 3, pp. 217-228, 1988.
[14] J.B. Mead, R.E. Mcintosh, D. Vandemark, and C.T. Swift, "Remote sensing of clouds and fog with a 1.4-mm radar," *Journal of Atmospheric and Oceanic Technology*, vol. 6, no. 6, pp. 1090-1097, 1989.
[15] K.B. Cooper, R. Rodriguez-Monje, L. Millán, M. Lebsock, S. Tanelli, J.V. Siles, C. Lee, and A. Brown, "Atmospheric humidity sounding using differential absorption radar near 183 GHz," *IEEE Geoscience and Remote Sensing Letters*, vol. 15, no. 2, pp. 163-167, 2018.
[16] R.J. Roy, M. Lebsock, L. Millán, R. Dengler, R. Rodriguez-Monje, J.V. Siles, and K.B. Cooper, "Boundary-layer water vapor profiling using differential absorption radar," *Atmospheric Measurement Techniques* vol. 11, no. 12, pp. 6511-6523, 2018.
[17] R.J. Roy, M. Lebsock, L. Millán, and K.B. Cooper, "Validation of a G-band differential absorption cloud radar for humidity remote sensing," *Journal of Atmospheric and Oceanic Technology*, submitted for publication.
[18] M.D. Lebsock, K. Suzuki, L. F. Millán, and P. M. Kalmus, "The feasibility of water vapor sounding of the cloudy boundary layer using a differential absorption radar technique," *Atmospheric Measurement Techniques* vol. 8, no. 9, pp. 3631-3645, 2015.
[19] L. Millán, M. Lebsock, N. Livesey, and S. Tanelli, "Differential absorption radar techniques: water vapor retrievals," *Atmospheric Measurement Techniques* vol. 9, no. 6, pp. 2633-2646, 2016.
[20] Read,W. G., Shippony, Z., Schwartz, M. J., Livesey, N. J., and Snyder, W. V.: The clear-sky unpolarized forward model for the EOS Microwave Limb Sounder (MLS), *IEEE Transactions on Geoscience and Remote Sensing*, vol. 44, pp. 1367–1379, 2006.
[21] J.V. Siles, K.B. Cooper, C. Lee, R.H. Lin, G. Chattopadhyay, and I. Mehdi, "A New Generation of Room-Temperature Frequency-Multiplied Sources With up to 10× Higher Output Power in the 160-GHz–1.6-THz Range," *IEEE Transactions on Terahertz Science and Technology* vol. 8, no. 6, pp. 596-604, 2018.
[22] K. Brown, A. Brown, T. Feenstra, D. Gritters, S. O'Connor, M. Sotelo, N. Kolias, K. C. Hwang, J. Kotce, and E. Robinson, "7kW GaN W-band transmitter," *2016 IEEE MTT-S International Microwave Symposium*, pp. 1-3, 2016.
[23] P. Kangaslahti, B. Lim, T. Gaier, A. Tanner, M. Varonen, L. Samoska, S. Brown, B. Lambrigtsen, S. Reising, J. Tanabe, O. Montes, D. Dawson, and C. Parashare, "Low noise amplifier receivers for millimeter wave atmospheric remote sensing," *2012 IEEE MTT-S International Microwave Symposium*, pp. 1-3, 2012.
[24] K.B. Cooper, "Imaging, doppler, and spectroscopic radars from 95 to 700 GHz," *Proc. SPIE* 9830, *Passive and Active Millimeter-Wave Imaging XIX, pp. 983005-1-9*, 2016.
[25] p. 684 in [5].
[26] J. Vivekanandan, S. Ellis, P. Tsai, Eric Loew, W-C. Lee, J. Emmett, M. Dixon, C. Burghart, and S. Rauenbuehler, "A wing pod-based millimeter wavelength airborne cloud radar," *Geoscientific Instrumentation, Methods and Data Systems*, vol. 4, no. 2, pp. 161-176, 2015.
[27] M.I. Skolnik, *Introduction to Radar Systems, 3rd Ed*. New York: McGraw-Hill, 2001.
[28] K.B. Cooper and G. Chattopadhyay, "Submillimeter-wave radar: Solid-state system design and applications," *IEEE Microwave Magazine*, vol. 15, no. 7, pp. 51-67, 2014.
[29] G.M. Brooker, "Understanding millimetre wave FMCW radars," *1st International Conference on Sensing Technology*, pp. 152-157, 2005.
[30] S.C. Reising, P. Kangaslahti, S.T. Brown, D.E. Dawson, A. Lee, D. Albers, O. Montes, T.C. Gaier, D.J. Hoppe, and B. Khayatian, "InP HEMT low-noise amplifier-based millimeter-wave radiometers from 90 to 180 GHz with internal calibration for remote sensing of atmospheric wet-path delay," *2012 IEEE MTT-S International Microwave Symposium*, pp. 1-3, 2012.
[31] K.B. Cooper, G. Chattopadhyay, R. Dengler, N. Llombart, R.E. Cofield, C. Lee, S. Filchenkov, and E. Koposova, "A grating-based circular polarization duplexer for submillimeter-wave applications," *IEEE Microwave and Wireless Components Letters*, vol. 22, no. 3, pp. 108-110, 2012.